arXiv:0904.4293v1 [physics.flu-dyn] 28 Apr 2009

Geophysical and Astrophysical Fluid Dynamics,
Vol. 100, Nos. 4–5, August–October 2006, 341–361
DOI:10.1080/03091920600784873

Parameter dependences of convection-driven dynamos in rotating spherical fluid shells

FRIEDRICH H. BUSSE∗† and RADOSTIN D. SIMITEV∗‡

∗ Institute of Physics, University of Bayreuth, D-95440 Bayreuth, Germany
‡ Department of Mathematical Sciences, The University of Liverpool, Liverpool L69 7ZL, UK

(*Received 28 April 2009; in final form ??*)

For the understanding of planetary and stellar dynamos an overview of the major parameter dependences of convection driven dynamos in rotating spherical fluid shells is desirable. Although the computationally accessible parameter space is limited, earlier work is extended with emphasis on higher Prandtl numbers and uniform heat flux condition at the outer boundary. The transition from dynamos dominated by non-axisymmetric components of the magnetic field to those dominated by the axisymmetric components depends on the magnetic Prandtl number as well as on the ordinary Prandtl number for higher values of the rotation parameter τ. The dependence of the transition on the latter parameter is also discussed. A variety of oscillating dynamos is presented and interpreted in terms of dynamo waves, standing oscillation or modified relaxation oscillations.

1. Introduction

Most global magnetic fields of planets and stars are generated by thermal or compositional convection in the deep interiors of those bodies. In spite of their common origin a large variety of dynamo processes is indicated by the observations of planetary and stellar magnetic fields. This is not surprising in view of the widely varying conditions under which dynamos operate. It is thus desirable to understand the effects of the most influential parameters on convection driven dynamos. The purpose of a study of the parameter dependence of dynamos would be twofold: On the one hand properties of observed magnetic fields could be explained in terms of parameter values of the respective system. On the other hand, unknown conditions in the interior of the celestial bodies may be inferred from the spatio-temporal structures of their magnetic fields. While it is not yet possible to create convincingly detailed models of planetary dynamos and of the solar cycle, some major variations of dynamos as function of their parameters can be explored through numerical simulations.

The increasing availability in recent years of computer capacity has facilitated large scale numerical simulations of the generation of magnetic fields by convection in rotating spherical fluid shells. Because of limited numerical resolution, molecular values of material properties are usually not attainable in computer simulations and eddy diffusivities representing the effects of the unresolved scales of the turbulent velocity field must therefor be invoked for comparisons with observations. It is often assumed for this reason that the eddy diffusivities for velocities, temperature and magnetic fields are identical. The effects of turbulence on the diffusion of vector and scalar quantities differ, however, and eddy diffusivity ratios such as the effective Prandtl number and the effective magnetic Prandtl number thus do not equal unity in general. Besides the Prandtl numbers, the boundary conditions exert a strong influence on convection and its dynamo action. Both effects will be considered in this paper.

† Email: `busse@uni-bayreuth.de`

In some respects this paper represents an extension of an earlier paper (Simitev and Busse, 2005, to which we shall refer to by SB05) which has focused on the dependence of average properties of convection driven dynamos on the Prandtl number. New results will be reported in the following and the emphasis will be placed on time dependent properties and on dynamo oscillations in particular. In addition the effect of boundaries of low thermal conductivity will be studied which are often more realistic than the commonly assumed boundaries with fixed temperature. Especially in the case of the Earth the low conductivity of the mantle will lead to a uniform heat flux from the core unless the effect of mantle convection is taken into account. Since the inhomogeneity introduced by the latter is not well known it will not be considered in the present analysis. For simulations with various inhomogeneous thermal boundary conditions see the papers by Glatzmaier *et al.* (1999) and by Olson and Christensen (2002). If compositionally driven convection in the Earth's core is emphasized the choice of uniform flux at the inner boundary and of fixed composition at the outer boundary is appropriate as has been assumed in the work of Glatzmaier and Roberts (1995).

After a brief introduction of the basic equations and the method of their numerical solution in section 2, some properties of convection without magnetic field will be considered in section 3. In particular the influence of fixed heat flux boundary conditions will be explored. In section 4 the onset of convection driven dynamos in fluids with different Prandtl numbers is described and in section 5 the oscillatory dynamos are interpreted in terms of the theory of dynamo waves. The influences of various boundary conditions are studied in section 6 and a concluding discussion is given in the final section 7.

2. Mathematical formulation of the problem and methods of solution

We consider a rotating spherical fluid shell of thickness d and assume that a static state exists with the temperature distribution $T_S = T_0 - \beta d^2 r^2/2$. Here $\beta = q/(3\,\kappa\, c_p)$ and $T_0 = T_1 - (T_2 - T_1)/(1-\eta)$, where T_1 and T_2 are the constant temperatures at the inner and outer spherical boundaries, $\eta = r_i/r_o$ is the radius ratio of the inner r_i to the outer r_o radius, q is the uniform heat source density, κ its thermal diffusivity, c_p is its specific heat at constant pressure and rd is the length of the position vector with respect to the center of the sphere. The gravity field is given by $\boldsymbol{g} = -d\gamma\boldsymbol{r}$. In addition to d, the time d^2/ν, the temperature $\nu^2/\gamma\alpha d^4$ and the magnetic flux density $\nu(\mu\varrho)^{1/2}/d$ are used as scales for the dimensionless description of the problem where ν denotes the kinematic viscosity of the fluid, ϱ its density and μ is its magnetic permeability. Since we shall assume the Boussinesq approximation material properties are regarded as constants except for the temperature dependence of the density described by $\alpha \equiv -(\,\mathrm{d}\varrho/\,\mathrm{d}T)/\varrho$ which is taken in the gravity term. Both, the velocity field $\boldsymbol{u}$ and the magnetic flux density $\boldsymbol{B}$, are solenoidal vector fields for which the general representation

$$\boldsymbol{u} = \nabla\times(\nabla v\times\boldsymbol{r}) + \nabla w\times\boldsymbol{r}, \tag{2.1a}$$

$$\boldsymbol{B} = \nabla\times(\nabla h\times\boldsymbol{r}) + \nabla g\times\boldsymbol{r}, \tag{2.1b}$$

can be employed. By multiplying the (curl)^2 and the curl of the Navier-Stokes equations of motion by $\boldsymbol{r}$ we obtain two equations for v and w,

$$[(\nabla^2-\partial_t)\mathcal{L}_2 + \tau\partial_\varphi]\nabla^2 v + \tau\mathcal{Q}w - \mathcal{L}_2\Theta = -\boldsymbol{r}\cdot\nabla\times[\nabla\times(\boldsymbol{u}\cdot\nabla\boldsymbol{u} - \boldsymbol{B}\cdot\nabla\boldsymbol{B})], \tag{2.2a}$$

$$[(\nabla^2-\partial_t)\mathcal{L}_2 + \tau\partial_\varphi]w - \tau\mathcal{Q}v = \boldsymbol{r}\cdot\nabla\times(\boldsymbol{u}\cdot\nabla\boldsymbol{u} - \boldsymbol{B}\cdot\nabla\boldsymbol{B}), \tag{2.2b}$$

where ∂_t denotes the partial derivative with respect to time t and where ∂_φ is the

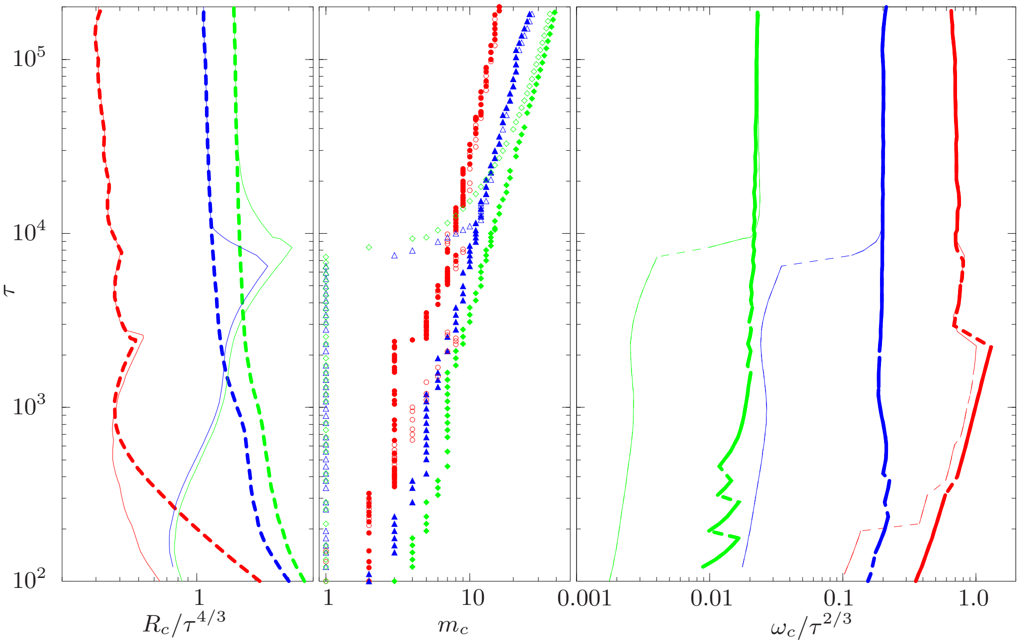

FIGURE 1. Critical values of the Rayleigh number R_c, wavenumber m_c and frequency ω_c as functions of τ in the case $\eta = 0.4$ for values of the Prandtl number $P = 0.2$ (red), $P = 2$ (blue), $P = 20$ (green) and UFBC (thick lines, filled symbols) and FTBC (thin lines, empty symbols).

partial derivative with respect to the angle φ of a spherical system of coordinates r, θ, φ. For further details we refer to SB05. The operators $\mathcal{L}_2$ and $\mathcal{Q}$ are defined by

$$\mathcal{L}_2 \equiv -r^2\nabla^2 + \partial_r(r^2\partial_r),$$

$$\mathcal{Q} \equiv r\cos\theta\nabla^2 - (\mathcal{L}_2 + r\partial_r)(\cos\theta\partial_r - r^{-1}\sin\theta\partial_\theta).$$

The heat equation for the dimensionless deviation Θ from the static temperature distribution can be written in the form

$$\nabla^2\Theta + R\mathcal{L}_2 v = P(\partial_t + \boldsymbol{u}\cdot\nabla)\Theta, \tag{2.3}$$

and the equations for h and g are obtained through the multiplication of equation of induction and of its curl by $\boldsymbol{r}$

$$\nabla^2\mathcal{L}_2 h = P_m[\partial_t\mathcal{L}_2 h - \boldsymbol{r}\cdot\nabla\times(\boldsymbol{u}\times\boldsymbol{B})], \tag{2.4a}$$

$$\nabla^2\mathcal{L}_2 g = P_m[\partial_t\mathcal{L}_2 g - \boldsymbol{r}\cdot\nabla\times(\nabla\times(\boldsymbol{u}\times\boldsymbol{B}))]. \tag{2.4b}$$

The Rayleigh number R, the Coriolis number τ, the Prandtl number P and the magnetic Prandtl number P_m are defined by

$$R = \frac{\alpha\gamma\beta d^6}{\nu\kappa}, \quad \tau = \frac{2\Omega d^2}{\nu}, \quad P = \frac{\nu}{\kappa}, \quad P_m = \frac{\nu}{\lambda}, \tag{2.5}$$

where λ is the magnetic diffusivity. For the static temperature distribution we have chosen the case of a homogeneously heated sphere. This state is traditionally used for the analysis of convection in self-gravitating spheres and offers the numerical advantage that for Rayleigh numbers close to the critical value R_c the strength of convection does not differ much near the inner and outer boundaries. As the Rayleigh number increases beyond R_c additional heat enters at the inner boundary and is delivered by convection to

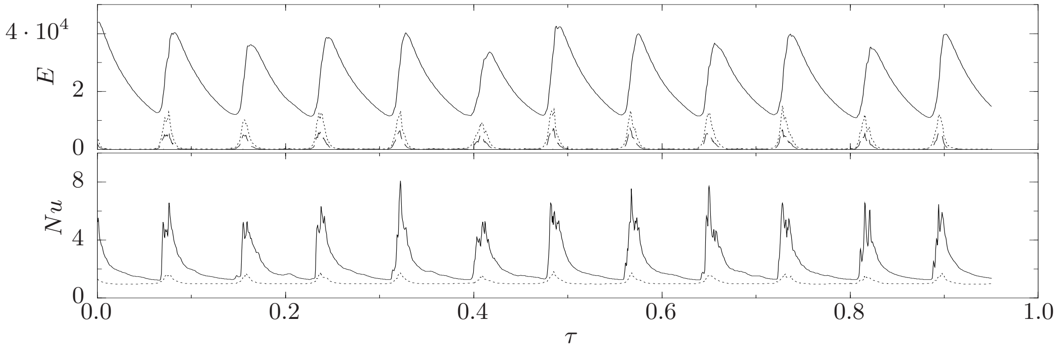

FIGURE 2. Time series of kinetic E energy densities (top) and Nusselt numbers Nu (bottom) for the convection case $P = 0.5$, $\tau = 1.5 \times 10^4$, $R = 1.5 \times 10^6$ and UFBC. The components $\overline{E}_t$ and Nu_o are represented by solid, $\check{E}_t$ and Nu_i by dotted lines and $\check{E}_p$ by a dashed line.

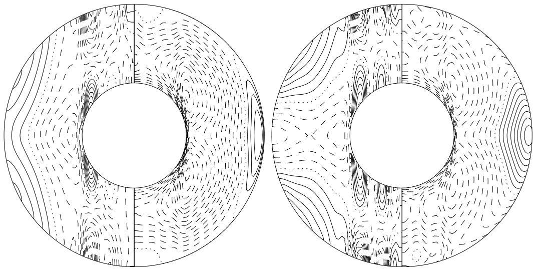

FIGURE 3. Isolines of azimuthally-averaged differential rotation $\overline{u_\varphi}$ (left half) and temperature perturbation $\overline{\Theta}$ (right half) in the case $P = 20$, $\tau = 10^4$, $R = 2 \times 10^6$ and FTBC (to the left) or UFBC (to the right). The fields represent averages in time.

the outer boundary. When R reaches a high multiple of R_c the heat generated internally in the fluid becomes negligible in comparison to the heat transported by convection through the spherical shell.

For the velocity field either stress-free boundaries,

$$v = \partial^2_{rr} v = \partial_r (w/r) = 0 \qquad \text{at } r = r_i \equiv \eta/(1-\eta) \text{ and } r = r_o \equiv 1/(1-\eta), \tag{2.6}$$

or no-slip boundaries,

$$v = \partial_r v = w = 0 \qquad \text{at } r = r_i \equiv \eta/(1-\eta) \text{ and } r = r_o \equiv 1/(1-\eta), \tag{2.7}$$

will be assumed. Unless indicated otherwise $\eta = 0.4$ and stress-free boundary conditions will be used in the following. The value $\eta = 0.4$ is not only employed because it turns out to be close to the radius ratio of the liquid outer core of the Earth, but because it also provides a good balance between the regions inside and outside the tangent cylinder touching the inner boundary at its equator. These two regions are known, of course, for their rather different dynamical properties.

For the thermal boundary conditions we shall assume that either the temperature is fixed (FTBC, i.e. Fixed Temperature Boundary Conditions),

$$\Theta = 0 \tag{2.8}$$

or its normal derivative is fixed (UFBC, i.e. Uniform Flux Boundary Conditions),

$$\frac{\partial}{\partial r}(\Theta - \overline{\overline{\Theta}}) = 0 \text{ , but } \quad \overline{\overline{\Theta}} = 0 \tag{2.9}$$

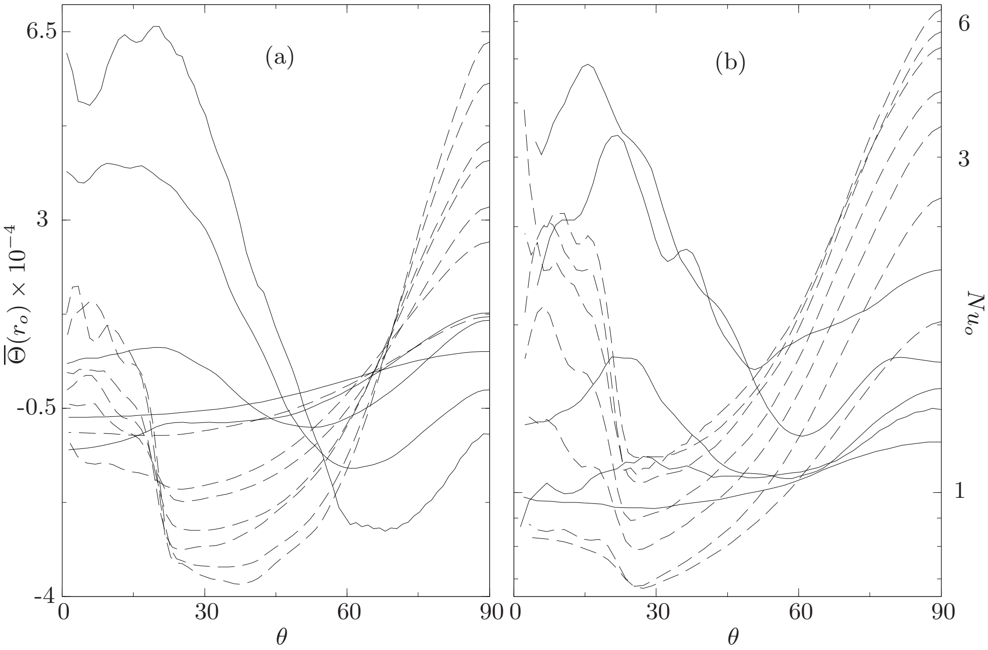

FIGURE 4. Time- and azimuthally-averaged temperature $\overline{\Theta}(r_o, \theta)$ in the case UFBC (left plot (a)) and Nusselt number $Nu_o(\theta)$ in the case FTBC (right plot (b)) at the outer boundary as a function of the colatitude θ for $P = 0.5$ with $\tau = 1.5 \times 10^4$ and $R = (10+5n) \times 10^5, n = 0...4$ from bottom to top at 0° (solid lines) and for $P = 20$ with $\tau = 10^4$ and $R = (10+5n) \times 10^5, n = 0...6$ from bottom to top at 90° (dashed lines). The temperature values $\overline{\Theta}(r_o, \theta)$ for $P = 0.5$ have been divided by 20.

at the boundary where the double overbar indicates the average over the spherical boundary. This latter definition has been used in order that the Rayleigh number continues to be based on the difference between the average temperatures between the boundaries.

For the magnetic field electrically insulating boundaries are assumed such that the poloidal function h must be matched to the function $h^{(e)}$ which describes the potential fields outside the fluid shell

$$g = h - h^{(e)} = \partial_r(h - h^{(e)}) = 0 \qquad \text{at } r \equiv \eta/(1-\eta) \text{ and } r \equiv 1/(1-\eta). \tag{2.10}$$

But computations for the case of an inner boundary with no-slip conditions and an electrical conductivity equal to that of the fluid have also been done. The numerical integration of equations (2.2),(2.3) and (2.4) together with boundary conditions (2.6) or (2.7) and (2.8) or (2.9) and (2.10) proceeds with the pseudo-spectral method as described by Tilgner and Busse (1997) and Tilgner (1999) which is based on an expansion of all dependent variables in spherical harmonics for the θ, φ-dependences, i.e.

$$v = \sum_{l,m} V_l^m(r,t) P_l^m(\cos\theta) \exp\{im\varphi\} \tag{2.11}$$

and analogous expressions for the other variables, w, Θ, h and g. P_l^m denotes the associated Legendre functions. For the r-dependence expansions in Chebychev polynomials are used. For further details see also Busse *et al.* (1998) or Grote *et al.* (2000). For the computations to be reported in the following a minimum of 33 collocation points in the radial direction and spherical harmonics up to the order 64 have been used. But in many

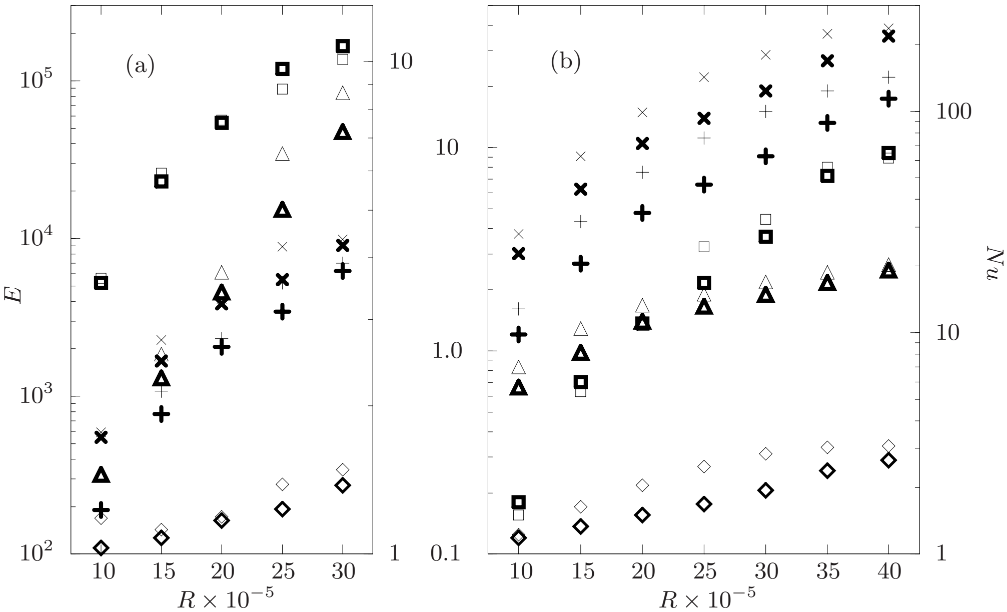

FIGURE 5. Kinetic E energy densities (left ordinate) and Nu (right ordinate) as functions of R for non-magnetic convection for (a) $P = 0.5$, $\tau = 1.5 \times 10^4$ and (b) $P = 20$, $\tau = 10^4$. The components $\overline{E}_t$, $\check{E}_p$, $\check{E}_t$ are represented by squares, plus-signs and crosses, respectively and Nu_o and Nu_i by diamonds and triangles. Cases with FTBC are shown with light symbols, and these with UFBC are shown with heavy symbols.

cases the resolution has been increased to 49 collocation points and spherical harmonics up to the order 96 or 128.

3. Convection in rotating spherical shells

For an introduction to the problem of convection in spherical shells we refer to the recent review of Busse (2002a). Additional information can be found in the papers by Grote and Busse (2001), Christensen (2002) and Simitev and Busse (2003, 2005). Here we shall focus the attention on the case of uniform heat flux boundary conditions. In figure 1 the critical value R_c of the Rayleigh number and the associated critical azimuthal wavenumber m_c have been plotted as a function of τ for several values of the Prandtl number P. The results for the case of fixed temperatures are shown for comparison. In the case of the steady onset of convection in a planar layer heated from below the critical value of the Rayleigh number and the associated wavenumber decrease monotonously with a decreasing thermal conductivity of a boundary (Sparrow *et al.*, 1964). There the onset of convection is described by a one-dimensional eigenvalue problem, while in the present case a two-dimensional problem in the complex domain must be solved because of the time dependent onset. Hence exceptions from the monotonous decrease of the critical values R_c, m_c in going from the fixed temperature to fixed flux boundary condition must be expected as are indeed found in the intermediate range of τ, $10^3 < \tau < 3 \times 10^4$. This phenomenon can also be recognized in the analytical results of Busse and Simitev (2004) obtained in the low Prandtl number limit. As the critical wavenumber m_c increases the value R_c becomes independent of the boundary conditions as must be anticipated since the r-dependence becomes negligible in comparison with the azimuthal dependence of

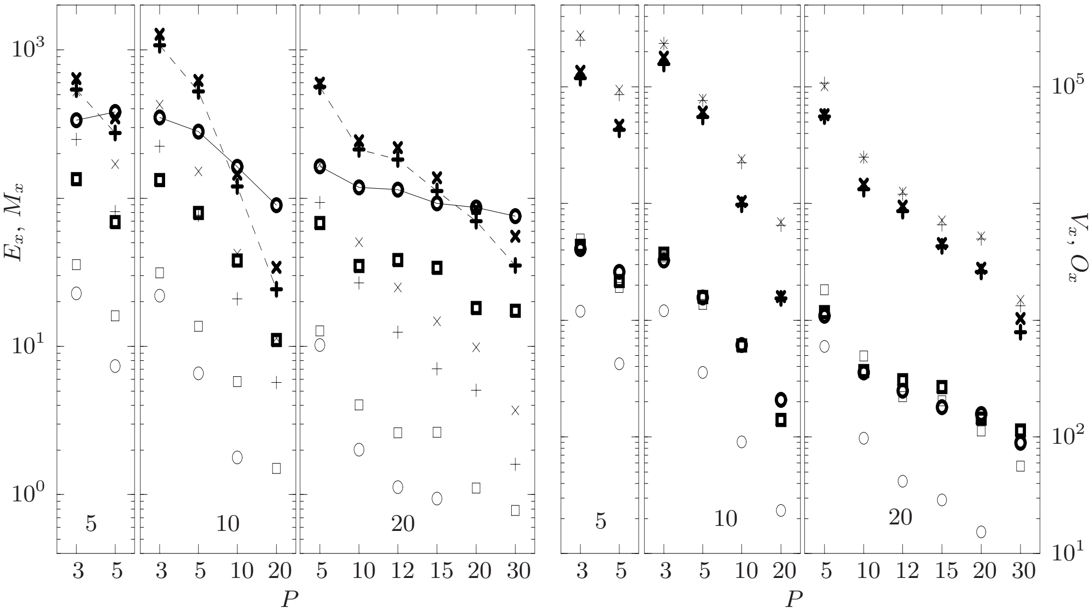

FIGURE 6. Kinetic E_x and magnetic M_x energy densities (left) and viscous V_x and Ohmic O_x dissipations (right) as functions of P for convection driven dynamos for $\tau = 10^4$, $R = 2 \times 10^6$, FTBC and magnetic Prandtl number as indicated in the boxes. The components $\overline{X}_p$, $\overline{X}_t$, $\check{X}_p$, $\check{X}_t$ (where $X = E, M, V, O$) are represented by circles, squares, plus-signs and crosses, respectively. Kinetic energy densities and viscous dissipations are shown with light symbols, magnetic energy densities and Ohmic dissipations are shown with heavy symbols. $\overline{E}_p$ is multiplied by a factor 20.

convection. The same independence is, of course, also evident in the asymptotic theory of Busse (1970).

At finite amplitudes convection in the presence of uniform heat flux boundaries evolves in a similar way as convection with fixed temperatures at the boundaries as long as the wavenumbers m_c of the two cases do not differ significantly. It should be mentioned here that in contrast to the linear results displayed in figure 1 only an outer uniform-flux boundary has been assumed for the computations of finite amplitude convection and its dynamos, while the fixed temperature condition has been kept at the inner boundary. This combination seems to be most appropriate for some planetary applications as mentioned in the Introduction.

The initial regime of drifting thermal Rossby waves is followed by the subsequent stages of vacillating convection, localized convection and relaxation oscillation that are observed with increasing Rayleigh number for Prandtl numbers of the order unity or less (but above values of P where convection in the form of inertial waves dominates, i.e. $P > 10/\sqrt{\tau}$ according to Ardes et al. (1996)). No significant influence of the thermal boundary conditions can be noticed. The relaxation oscillations shown in figure 2 seem to be a little more pronounced than in the case of a fixed temperature outer boundary, but are otherwise identical. At higher Prandtl numbers a stronger tendency towards the thermal wind type of differential rotation can be noticed in the presence of a uniform-flux thermal boundary as seen in figure 3. This is a consequence of the stronger latitudinal temperature gradient admitted by the insulating boundary condition.

At finite amplitudes of convection the heat transport is of special interest the efficiency of which is measured by the Nusselt number. This is defined as the heat transport in

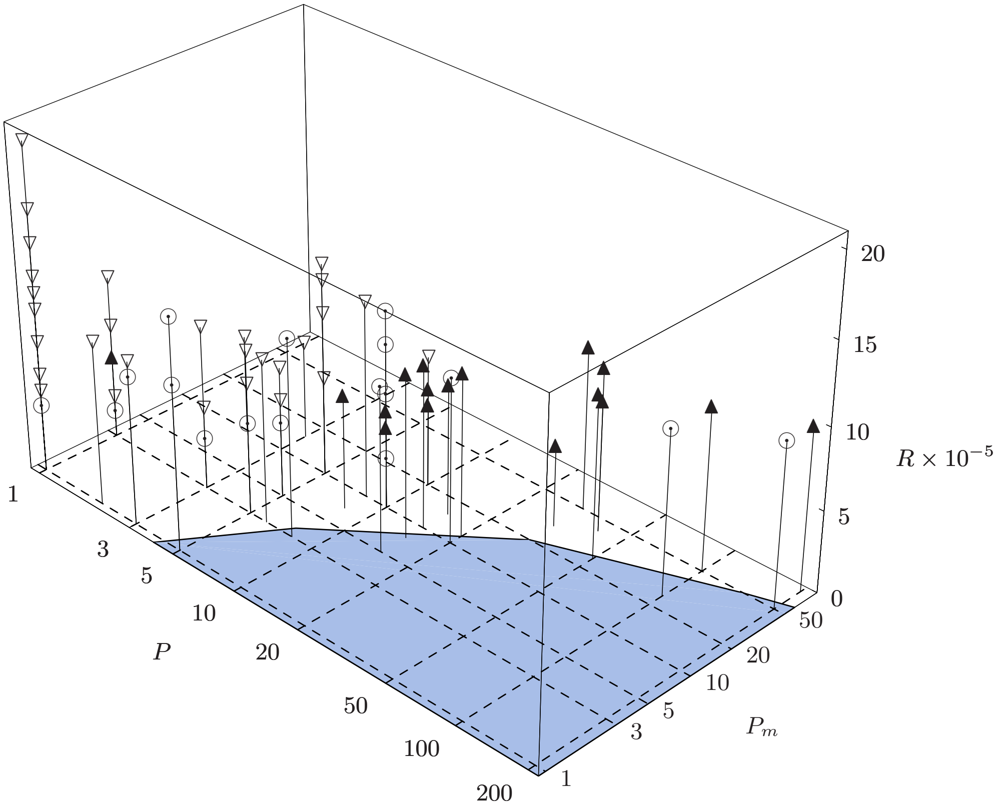

FIGURE 7. Convection-driven dynamos as function of R, P and P_m for $\tau = 5\times10^3$. The symbols indicate dynamos for which $\overline{M}_p < \check{M}_p$ (▽), those for which opposite is true (▲) and decaying dynamos (⊙).

the presence of convection divided by the heat transport in the absence of motion. In the case of the spherical fluid shell two Nusselt numbers can be defined measuring the efficiency of convection at the inner and the outer boundary,

$$Nu_i = 1 - \frac{P}{r_i}\left.\frac{d\overline{\overline{\Theta}}}{dr}\right|_{r=r_i} \qquad Nu_o = 1 - \frac{P}{r_o}\left.\frac{d\overline{\overline{\Theta}}}{dr}\right|_{r=r_o} \tag{3.1}$$

where the double bar indicates the average over the spherical surface. In addition the local Nusselt numbers as function of latitude

$$Nu_i(\theta) = 1 - \frac{P}{r_i}\left.\frac{d\overline{\Theta}}{dr}\right|_{r=r_i} \qquad Nu_o(\theta) = 1 - \frac{P}{r_o}\left.\frac{d\overline{\Theta}}{dr}\right|_{r=r_o} \tag{3.2}$$

are of interest where only the azimuthal average is applied, as indicated by the single bar. The latitudinal dependence of the local Nusselt number and of the azimuthally averaged temperature at the outer boundary are shown in figure 4 for the cases of fixed temperature conditions (right) and uniform flux conditions (left) in the cases $P = 0.5$ and $P = 20$. As must be expected latitudes of high temperatures at the boundary correspond to those with high values of $Nu_o(\theta)$. This figure demonstrates that at low supercritical Rayleigh numbers the heat transport occurs primarily across the equatorial region, but as

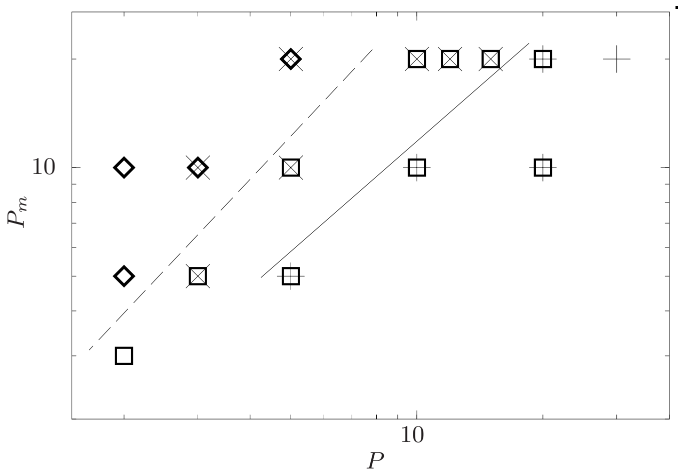

FIGURE 8. Convection-driven dynamos as function of P and P_m with $\tau = 10^4$ and $R = 2 \times 10^6$ (light symbols) and with $\tau = 3 \times 10^4$ and $R = 3.5 \times 10^6$ (heavy symbols). The dynamos for which $\overline{M}_p > \check{M}_p$ are indicated by squares in the case of $\tau = 3 \times 10^4$ and by plus-signs in the case of $\tau = 10^4$. The dynamos for which $\overline{M}_p < \check{M}_p$ are indicated by diamonds in the case of $\tau = 3 \times 10^4$ and by crosses in the case of $\tau = 10^4$. The broken and the solid lines represent the approximate location of the parameter values where the transition from $\check{M}_p$-dominated to $\overline{M}_p$-dominated dynamos occurs for $\tau = 3 \times 10^4$ and $\tau = 10^4$, respectively.

R increases the heat transport in the polar regions takes off, especially in the case of the lower value of P, and soon exceeds that at low latitudes. In the polar regions convection is better adjusted for carrying heat from the lower boundary to the upper one, and it is known from computations of the convective heat transport in horizontal layers rotating about a vertical axis that the value of Nu may exceed the value in a non-rotating layer at a given value of R in spite of the higher critical Rayleigh number in the former case.

At higher values of the Prandtl number the takeover of the heat transport by convection in the polar regions is less pronounced, but the contrast between the equatorial region and the mid-latitudes is even stronger than for lower values of P. Again, a dramatic difference between fixed flux and fixed temperature boundary conditions can not be discerned.

It is also useful to compare the averages over space and time of the kinetic energy densities of the various components of the convection flow. They are defined by

$$\overline{E}_p = \frac{1}{2}\langle| \nabla \times (\nabla \bar{v} \times \boldsymbol{r}) |^2\rangle, \quad \overline{E}_t = \frac{1}{2}\langle| \nabla \bar{w} \times \boldsymbol{r} |^2\rangle, \tag{3.3a}$$

$$\check{E}_p = \frac{1}{2}\langle| \nabla \times (\nabla \check{v} \times \boldsymbol{r}) |^2\rangle, \quad \check{E}_t = \frac{1}{2}\langle| \nabla \check{w} \times \boldsymbol{r} |^2\rangle, \tag{3.3b}$$

where the angular brackets indicate the average over the fluid shell and over time and $\bar{v}$ refers to the azimuthally averaged component of v, while $\check{v}$ is defined by $\check{v} = v - \bar{v}$. In figure 5 the growth of these energies with the the Rayleigh number is shown for both, the case with an insulating and the case with a fixed temperature at the outer boundary. In the low Prandtl number case of the left diagram the rapid growth with R of $\overline{E}_t$ corresponding to the energy of differential rotation is remarkable. Only for higher values of P does $\overline{E}_t$ never exceed the energies of the fluctuating components of motion.

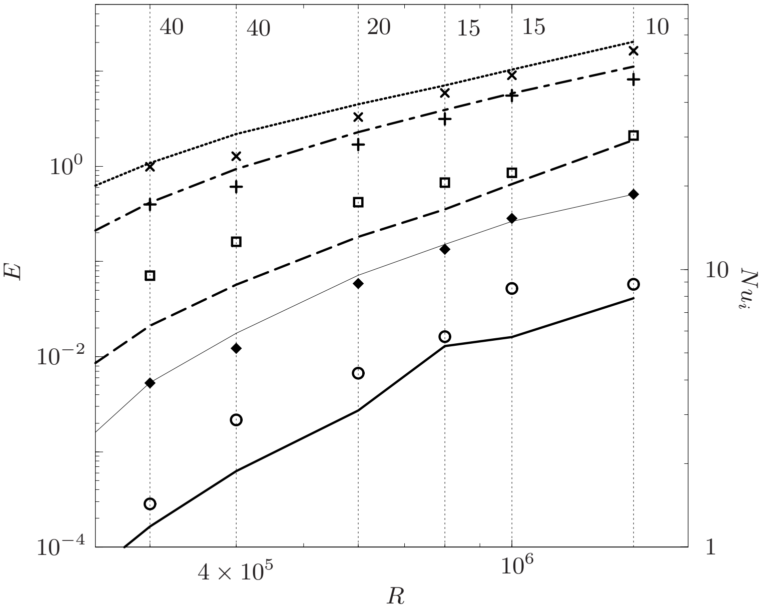

FIGURE 9. Time-averaged kinetic energy densities $\overline{E}_p$, (solid line and circles), $\overline{E}_t$ (dashed line and squares), $\check{E}_p$ (dashed-dotted line and plus-signs), $\check{E}_t$ (dotted line and crosses) and Nusselt number Nu_i (thin line and solid diamonds) of non-magnetic convection (lines) and dynamo solutions (symbols) for $P = 20$, $\tau = 5 \times 10^3$ and R as indicated at the x-axis. The symbols connected by the dotted lines correspond to the values of P_m given at the top of the figure.

4. Convection-driven dynamos

The onset convection-driven dynamos as function of parameters equivalent to those given by expressions (2.5) has been investigated in numerous papers, see, for example, Busse *et al.* (1998), Christensen *et al.* (1999), Grote *et al.* (2000, 2001), Grote and Busse (2001), Kutzner and Christensen (2000, 2002), SB05. For displays of dynamo onsets as functions of P, R and τ see SB05 and Busse (2002). Typically the Rayleigh number required for dynamos increases with decreasing P_m such that the minimum magnetic Reynolds number Rm defined by $Rm = (2E)^{1/2} P_m$ stays constant at a value of the order 10^2. As has been found before (Christensen *et al.* 1999; SB05) a too high value of Rm can be detrimental for dynamos because of flux expulsion from the convection eddies. Especially at Prandtl numbers of the order unity or somewhat lower a finite amplitude of the magnetic field is required for dynamos close to their minimum value of R since the velocity field modified by the action of the Lorentz force is more suitable for dynamo action, mainly through the suppression of the differential rotation (Grote and Busse, 2001), than the non-magnetic velocity field. In a statistical sense convection-driven dynamos thus usually correspond to saddle node bifurcations.

In SB05 it has been noted that a transition from dynamos dominated by non-axisymmetric components of the magnetic field to those dominated by the axisymmetric poloidal field occurs with increasing Prandtl number when a value $P = P_t \sim 8$ is reached in the case $\tau = 5 \times 10^3$. In figure 6 results are displayed for the case $\tau = 10^4$ which also exhibit this transition. The magnetic energies $\overline{M}_p$, $\overline{M}_t$, $\check{M}_p$, $\check{M}_t$ are defined in analogy to the definitions (3) for the kinetic energies with h and g replacing v and w. For $P < P_t$, $\overline{M}_p < \check{M}_p$ holds and for $P > P_t$ the opposite is true. The results of figure 6 demonstrate that the transition Prandtl number P_t depends strongly on P_m with higher values of P_m favoring higher values of P_t. For this reason a more complete analysis of the transition in the

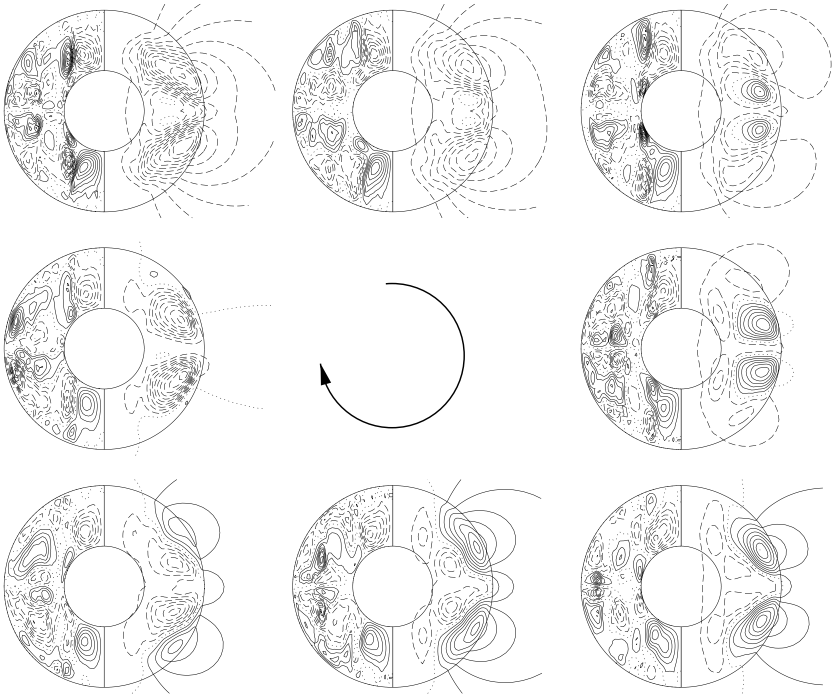

FIGURE 10. A period of dipolar oscillations for $P = 5$, $\tau = 5 \times 10^3$, $R = 6 \times 10^5$, $Pm = 10$ with $\Lambda = 0.1429$. The plots start at the upper left corner and follow clockwise with $\Delta t = 0.035$ and show meridional lines of constant $\overline{B_\varphi}$ in the left half and of $r \sin\theta \partial_\theta \overline{h}$ =const. in the right half of each circle.

case $\tau = 5 \times 10^3$ has been made with the inclusion of the Rayleigh number. The results shown in figure 7 indicate that the parameter P_m appears to have a lesser influence on P_t at $\tau = 5 \times 10^3$ than at $\tau = 10^4$. The trend that with increasing τ the value of P_t decreases is confirmed in figure 8 where results obtained for $\tau = 3 \times 10^4$ and for $\tau = 10^4$ are compared. In each of the two cases the Rayleigh number R has been kept constant. While the energies of the axisymmetric components of the magnetic field increase relative to those of the non-axisymmetric components with increasing P, only a weak tendency in this direction can be noticed in the corresponding Ohmic dissipations.

In SB05 the increase in the efficiency of convection in the presence of a dynamo generated magnetic field has been demonstrated for Prandtl numbers of the order unity or less. At higher Prandtl numbers the magnetic field is no longer needed to oppose the destructive (for the convective heat transport) effects of the differential rotation which manifest themselves, for instance, in the relaxation oscillations shown in figure 2. When Nusselt numbers and kinetic energies are thus compared for $P = 20$ in figure 9 for convection with and without a dynamo, little change is seen. The energy of differential rotation even appears to be slightly larger in the magnetic case.

5. Oscillatory dynamos

It has long been known that mean-field dynamos in the presence of a strong differential rotation typically occur in the form of oscillatory dynamos, especially if any meridional circulation is relatively weak (Roberts, 1972). In the present case of dynamos driven by turbulent convection nearly time periodic oscillations are a persistent feature in the

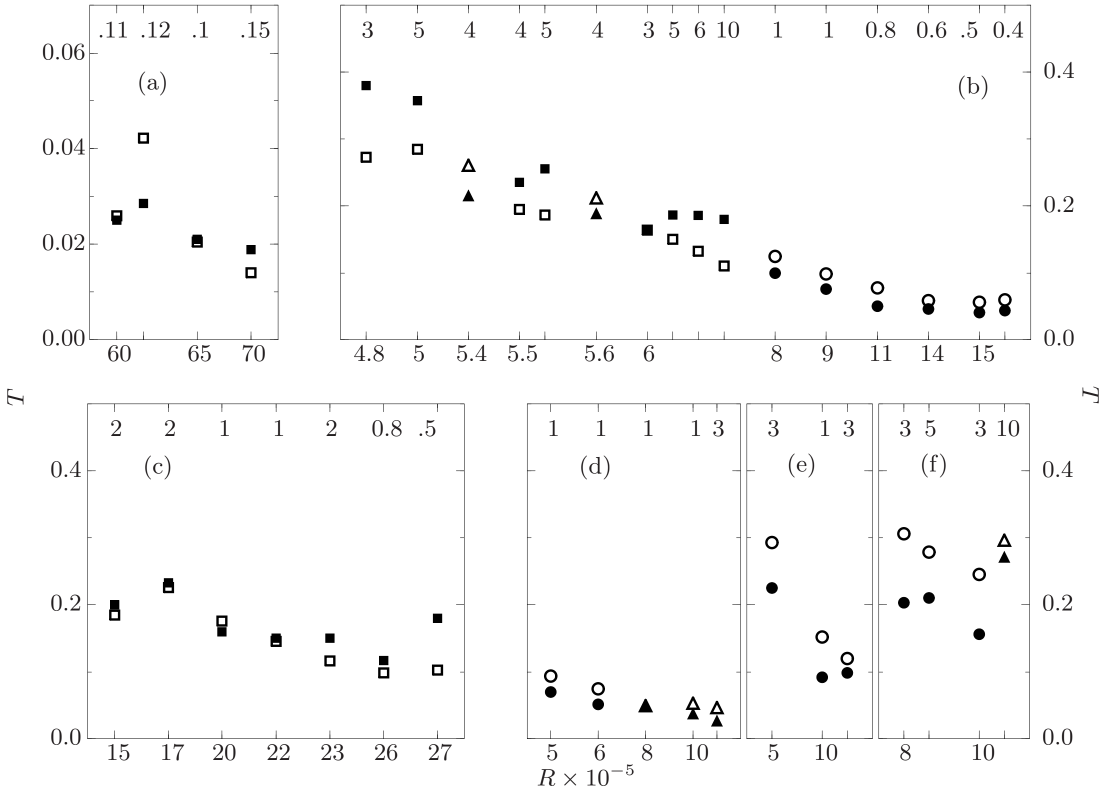

FIGURE 11. Period of dynamo oscillations T obtained from the analytical expression (5.8) (empty symbols) and from simulations (solid symbols) for (a) $P = 0.1$, $\tau = 10^5$, (b) $P = 1$, $\tau = 10^4$, (c) $P = 1$, $\tau = 3 \times 10^4$ and (d) $P = 1$, (e) $P = 3$, (f) $P = 5$ and $\tau = 5 \times 10^3$. The values of R are given at the x-axis and the values of P_m are given at the top of the panels. The symbols indicate quadrupolar (circles), hemispherical (squares) and dipolar (triangles) dynamos.

case of hemispherical and quadrupolar dynamos. Typical examples have been presented by Grote et al. (1999) and Grote and Busse (2000). Oscillatory dynamos with dipolar symmetry are less frequently encountered. An example is shown in figure 10. Since the prograde differential rotation increases with radius r the oscillations assume the form of two symmetric dynamo waves propagating from the equator to high latitudes where they decay similarly as found in mean-field dynamos.

For the theoretical description of these waves we follow Parker's (1955) plane layer model with the (x, y, z)-coordinates corresponding to the $(\varphi, -\theta, r)$-directions in the spherical shell. With the ansatz

$$\boldsymbol{B} = \boldsymbol{B}_p + \boldsymbol{i}B, \quad \boldsymbol{B}_p = \nabla \times \boldsymbol{i}A, \quad \boldsymbol{v} = \boldsymbol{i}\,U + \check{\boldsymbol{v}}, \tag{5.1}$$

where $\boldsymbol{i}$ is the unit vector in the x-direction and where the fields A, B are x-independent, U depends only on z and the x, y-average of $\check{\boldsymbol{v}}$ vanishes. Using Parker's equations in dimensionless form,

$$\frac{\partial}{\partial t}A = \hat{\alpha}B + \nabla^2 A/P_m, \quad \frac{\partial}{\partial t}B = \boldsymbol{B}_p \cdot \nabla U + \nabla^2 B/P_m, \tag{5.2}$$

we may obtain solutions of the form

$$(A, B) = (\hat{A}, \hat{B}) \exp[i\boldsymbol{q} \cdot \boldsymbol{x} + \sigma t]. \tag{5.3}$$

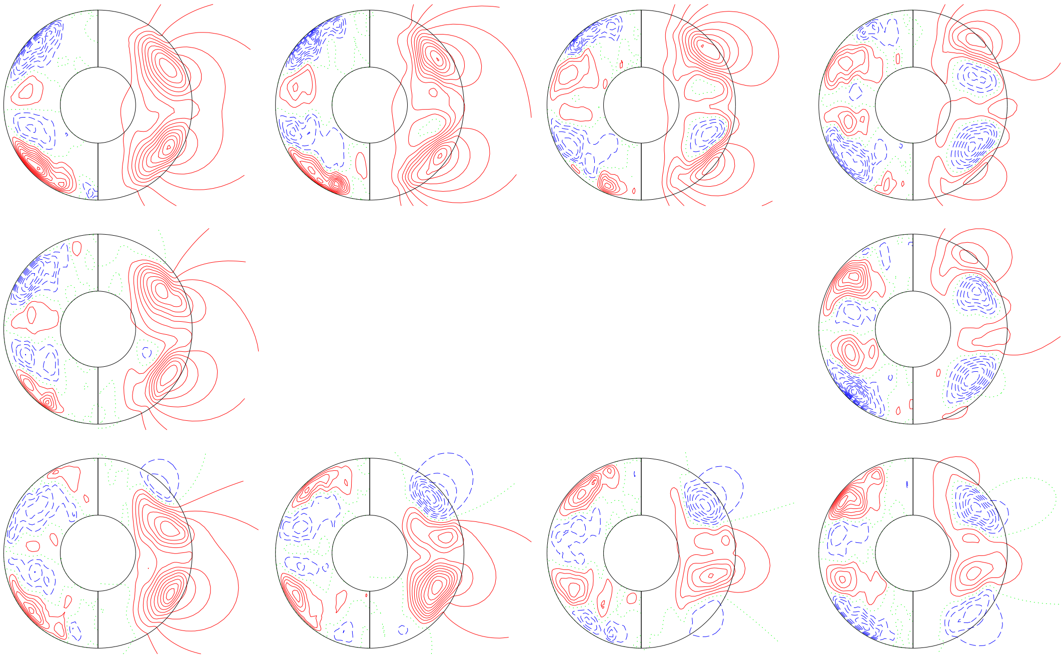

FIGURE 12. A period of dipolar oscillations for $P = 1$, $\tau = 5 \times 10^3$, $R = 10^6$, $Pm = 1$ with $\Lambda = 0.6794$. The plots start at the upper left corner and follow clockwise with $\Delta t = 0.0051$ and show isolines similar to those in figure 10.

The equations are satisfied with

$$p\hat{A} = \hat{\alpha}\hat{B}, \quad p\hat{B} = -i(\boldsymbol{q} \times \nabla U)_x \hat{A} \quad \text{with} \quad p = \sigma + |\boldsymbol{q}|^2/P_m \tag{5.4}$$

and with the resulting dispersion relation

$$p^2 = 2i\Gamma \equiv 2i(-\hat{\alpha}(\boldsymbol{q} \times \nabla U)_x/2). \tag{5.5}$$

The latter yields the growth rates

$$\sigma = \begin{cases} -|\boldsymbol{q}|^2/P_m \pm \sqrt{\Gamma} \pm i\sqrt{\Gamma} & \text{for} \quad \Gamma > 0, \\ -|\boldsymbol{q}|^2/P_m \pm \sqrt{|\Gamma|} \mp i\sqrt{|\Gamma|} & \text{for} \quad \Gamma < 0. \end{cases} \tag{5.6}$$

Growing waves are found for $\mp\hat{\alpha}q_y dU/dz > 2|\boldsymbol{q}|^4/P_m^2$ with the wave propagating in the $\mp y$-direction provided that q_y and dU/dz are positive quantities. Here the upper (lower) sign refers to the case $\Gamma > 0$ ($\Gamma < 0$).

The coefficient $\hat{\alpha}$ is related to the helicity of the convection flow,

$$\hat{\alpha} \equiv -\frac{1}{3P_m}\int\int \frac{\hat{q}^2 F(\hat{q},\omega)}{\omega^2 + \hat{q}^4/P_m^2} d\hat{q}d\omega \approx -\frac{P_m}{3\hat{q}^2}\int\int F(\hat{q},\omega)d\hat{q}d\omega \equiv -\frac{P_m}{3\hat{q}^2}\langle \check{\boldsymbol{v}} \cdot \nabla \times \check{\boldsymbol{v}} \rangle. \tag{5.7}$$

where $F(\hat{q},\omega)$ is the helicity spectrum function (Moffatt, 1978) which is assumed to have a peak at the typical wavenumber $\hat{q}$ with $\hat{q}^2/P_m \gg |\omega|$. $\hat{q}$ will typically exceed the value $|\boldsymbol{q}|$ used in expression (5.3). But if we use an average value $q_y \approx \hat{q} \approx 2\pi/d$, we find for the dimensionless frequency ω,

$$\omega \approx \frac{1}{2\pi}\left(P_m \frac{\pi}{3}\langle \check{\boldsymbol{v}} \cdot \nabla \times \check{\boldsymbol{v}} \rangle \sqrt{2\overline{E_t}}\right)^{1/2}. \tag{5.8}$$

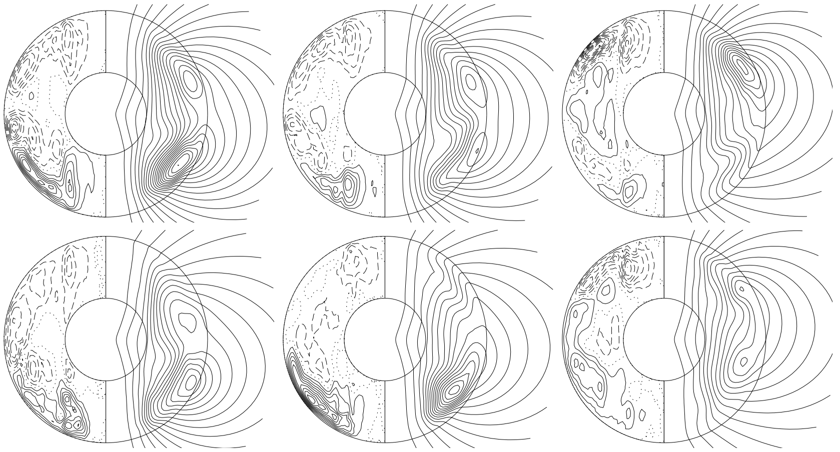

FIGURE 13. Same as figure 10 but for $P = 0.05$, $\tau = 10^5$, $R = 4\times10^6$, $P_m = 0.3$ with $\Lambda = 1.1364$. with $\Delta t = 0.0035$. The time series of plots starts with the upper left plot and continues in the clockwise sense.

Periods corresponding to this value of ω are presented for several dipolar, hemispherical and quadrupolar dynamos in figure 11 where they can be compared with periods obtained from the dynamo simulations. For this purpose the helicity $\langle \check{\boldsymbol{v}} \cdot \nabla \times \check{\boldsymbol{v}} \rangle$ was obtained as an average over time and over either the northern or the southern hemisphere. Even though the expression (5.8) represents only a crude estimate it seems to fit the various oscillatory dynamos quite well. The agreement between mean-field theory and numerical simulation is due to the dominant action of the differential rotation in creating the axisymmetric toroidal magnetic flux. As discussed in more detail in SB05 the α-effect of mean-field theory is usually not clearly noticeable in numerical simulations in contrast to the ω-effect (see also Schrinner *et al.*. 2005)

Because the Prandtl number is moderately large in the case of figure 10 the typical polar flux tubes have formed which do not participate in the oscillation. The axisymmetric poloidal field, however, participates fully in the oscillation and exhibits about equal amplitudes for both polarities. This property is often missing as shown in figure 12 where the red field lines dominate and a dipole field with the opposite polarity does not become established throughout the cycle. Finally, an extreme version of the latter situation is found in the case of the so-called "invisibly" oscillating dynamos (Busse and Simitev, 2005). A typical example is found when the magnetic Prandtl number is somewhat lower than in the case of figure 10 such that the polar flux tubes are much stronger and the oscillation of the axisymmetric poloidal field is suppressed. As a result external observers will not be able to recognize the oscillation of the axisymmetric toroidal field outside the tangent cylinder.

Besides the oscillations related to traveling dynamo waves other types of oscillations may be noticed. Typical for Prandtl numbers of the order unity or less are global oscillations in which a nearly hemispherical field switches periodically the hemispheres as shown in figure 13. This behavior reminds one of similar, but much weaker oscillations with a period of about 3.6 years which have been reported for the solar magnetic field (Knaack *et al.* 2004). According to the observations the flux emerging from the solar southern hemisphere periodically exceeds that from the northern hemisphere and vice versa.

While the dynamo oscillations can be well understood in terms of the linear Parker model, they actually occur at finite amplitudes of the magnetic field. As a measure of

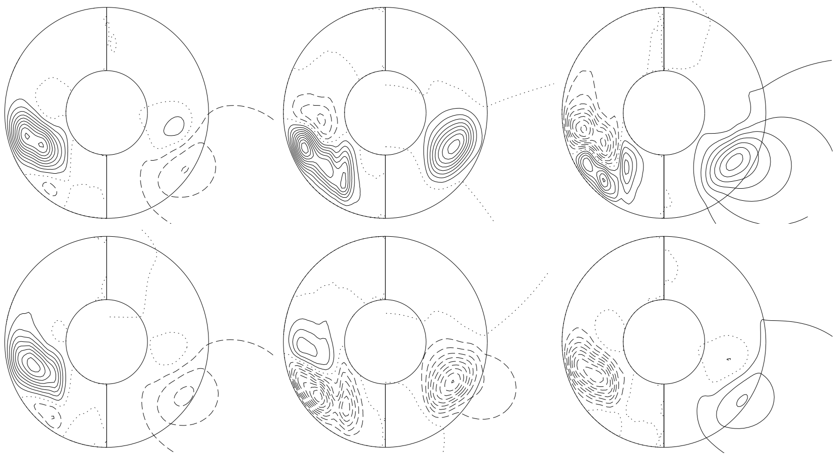

FIGURE 14. A period of hemispherical oscillations for $P = 0.1$, $\tau = 10^5$, $R = 6 \times 10^6$, $P_m = 0.11$ with $\Lambda = 0.1424$. The plots follow clockwise with $\Delta t = 0.005$ and show isolines similar to those in figure 10.

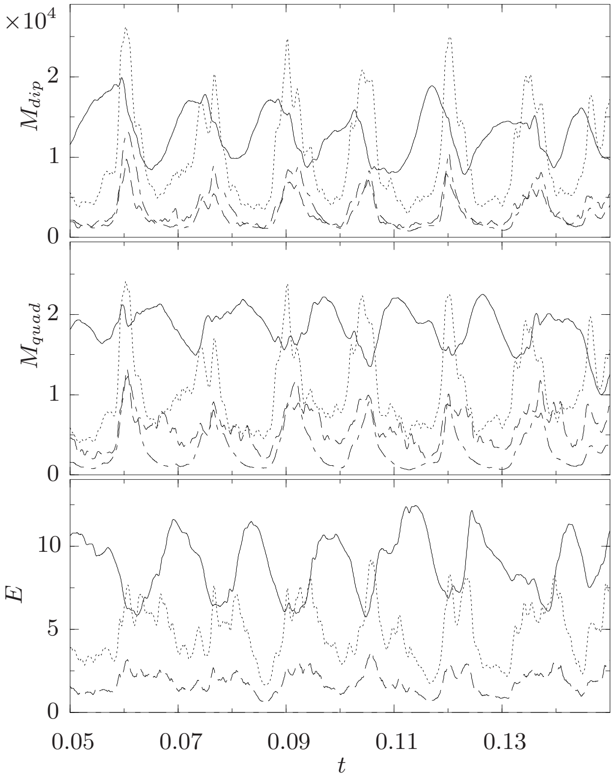

FIGURE 15. Time series of energy densities of a hemispherical dynamo in the case $P = 0.1$, $\tau = 10^5$, $R = 6 \times 10^6$, $P_m = 0.11$. The upper and middle panels show energy densities of dipolar and quadrupolar components of the magnetic field, while the lower panel shows energy densities of the velocity field. The mean toroidal components are represented by solid lines, the fluctuating toroidal - by dotted lines, the mean poloidal - by dot-dashed lines and the fluctuating poloidal by dashed lines.

the latter we have denoted the Elsasser number Λ in the captions of figures 10, 12, 13

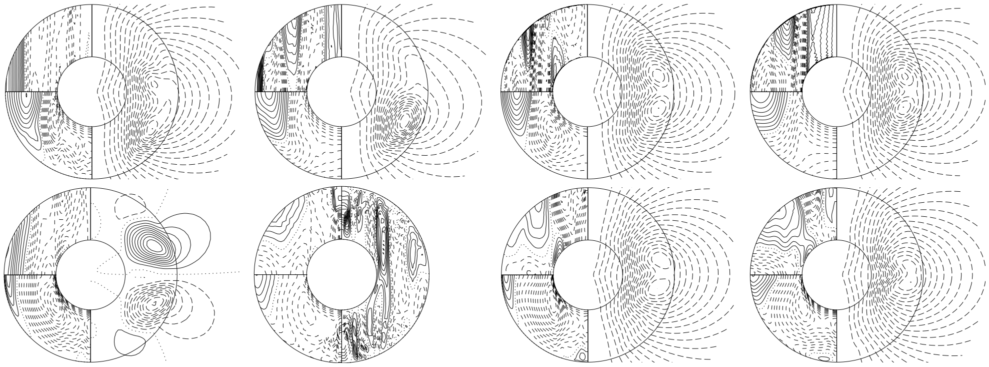

FIGURE 16. The dynamo cases (a) to (h) presented in table 1 (from left to right, first row then second row). In each plot the upper left quarter shows the differential rotation $\overline{u}_\varphi$, the lower left quarter shows the temperature perturbation $\overline{\Theta}$ and the right half shows the meridional field lines $r\sin\theta\partial_\theta\overline{h}$ =const. The plot of case (f) shows the meridional streamlines $r\sin\theta\partial_\theta\overline{v}$ =const. to the right.

and 14. The Elsasser number is defined by

$$\Lambda = \frac{2MP_m}{\tau} \tag{5.9}$$

where M denotes the magnetic energy density averaged over the fluid shell and in time, i.e. $M = \overline{M}_p + \overline{M}_t + \check{M}_p + \check{M}_t$. The interaction between magnetic and velocity field has been taken into account in expression (5.8), of course, in that the actual values for $\overline{E_t}$ and the helicity have been used in its evaluation. An even stronger interaction with the velocity field is found in the case of figure 14 where a coupling with relaxation oscillations of convection similar to those shown in figure 2 occurs. The period, however, is still comparable to that of the dynamo waves discussed above. These oscillations are typical for hemispherical dynamos of the kind shown in figure 14 as is evident from figure 11(a). Hardly a full wavelength of the standing dynamo wave participates in the oscillation in this case and thus the amplitude of the mean poloidal field varies throughout the cycle. Accordingly the Lorentz force restraining the differential rotation varies as well. The differential rotation thus participates in the oscillation and the other components of the velocity field affected by its shearing action do so as well as can clearly be seen in the time record of the kinetic and magnetic energies displayed in figure 15 for the same case as shown in figure 14.

6. Dynamos for different boundary conditions

All dynamos discussed so far in the preceding sections have been computed for stress-free boundaries with fixed temperatures. In this section some convection-driven dynamos obtained for other boundary conditions are considered. They have been listed in table 1. As must be expected on the basis of the results shown in figure 5 the strength of convection with fixed heat flux outer boundary is lower than in the case of the fixed temperature condition. This property is reflected in the corresponding dynamos where the kinetic and magnetic energies in cases B are usually less than those in cases A except for the differential rotation and the associated mean toroidal magnetic field.

Of particular interest are the comparisons of cases with and without magnetic fields. Values for the latter cases have been added in table 1 in brackets wherever they were available. In the cases (a) and (b) the numerical resolution turned out to be insufficient in

Case	(a)	(b)	(c)	(d)	(e)	(f)	(g)	(h)
	$P = 0.1,\ \tau = 10^5,\ R = 4 \times 10^6,\ P_m = 0.5$				$P = 5,\ \tau = 5 \times 10^3$ $R = 8 \times 10^5,\ P_m = 3$		$P = 20,\ \tau = 10^4$ $R = 2 \times 10^6,\ P_m = 20$	
BC	**A**	**B**	**C**	**D**	**A**	**B**	**A**	**B**
Type	D	D	D	D	Q	–	D	D
$\overline{E}_p$	0.286×10^2	0.258×10^2	0.112×10^2 (0.937×10^2)	0.530×10^1	0.157 (0.147)	0.166	0.018 (0.012)	0.026 (0.017)
$\overline{E}_t$	0.599×10^4	0.641×10^4	0.647×10^3 (0.758×10^5)	0.950×10^3	0.533×10^2 (0.113×10^3)	0.176×10^2	0.114×10^1 (0.141×10^1)	0.166×10^1 (0.140×10^1)
$\check{E}_p$	0.142×10^5	0.109×10^5	0.115×10^5 (0.221×10^5)	0.576×10^4	0.574×10^2 (0.545×10^2)	0.393×10^2	0.500×10^1 (0.758×10^1)	0.361×10^1 (0.433×10^1)
$\check{E}_t$	0.336×10^5	0.273×10^5	0.257×10^5 (0.540×10^5)	0.139×10^5	0.119×10^3 (0.117×10^3)	0.867×10^2	0.985×10^1 (0.149×10^2)	0.777×10^1 (0.952×10^1)
$\overline{M}_p$	0.129×10^5	0.109×10^5	0.392×10^5	0.305×10^5	0.487×10^1	–	0.886×10^2	0.104×10^3
$\overline{M}_t$	0.133×10^5	0.102×10^5	0.879×10^4	0.104×10^5	0.325×10^1	–	0.184×10^2	0.260×10^2
$\check{M}_p$	0.136×10^5	0.100×10^5	0.169×10^5	0.112×10^5	0.818×10^1	–	0.702×10^2	0.723×10^2
$\check{M}_t$	0.307×10^5	0.264×10^5	0.345×10^5	0.257×10^5	0.109×10^2	–	0.865×10^2	0.871×10^2
$\overline{V}_p$	0.643×10^5	0.529×10^5	0.104×10^6 (0.108×10^8)	0.795×10^5	0.151×10^3 (0.140×10^3)	0.183×10^3	0.152×10^2 (0.165×10^2)	0.410×10^2 (0.202×10^2)
$\overline{V}_t$	0.584×10^6	0.608×10^6	0.366×10^6 (0.280×10^8)	0.295×10^6	0.182×10^4 (0.324×10^4)	0.936×10^3	0.114×10^3 (0.134×10^3)	0.142×10^3 (0.179×10^3)
$\check{V}_p$	0.133×10^8	0.956×10^7	0.179×10^8 (0.446×10^8)	0.890×10^7	0.414×10^5 (0.390×10^5)	0.311×10^5	0.493×10^4 (0.909×10^4)	0.356×10^4 (0.467×10^4)
$\check{V}_t$	0.229×10^8	0.176×10^8	0.354×10^8 (0.819×10^8)	0.182×10^8	0.455×10^5 (0.445×10^5)	0.378×10^5	0.524×10^4 (0.964×10^4)	0.409×10^4 (0.613×10^4)
$\overline{O}_p$	0.626×10^6	0.490×10^6	0.129×10^7	0.109×10^7	0.544×10^3	–	0.316×10^4	0.375×10^4
$\overline{O}_t$	0.148×10^7	0.132×10^7	0.944×10^6	0.858×10^6	0.359×10^3	–	0.290×10^4	0.438×10^4
$\check{O}_p$	0.125×10^8	0.855×10^7	0.138×10^8	0.738×10^7	0.468×10^4	–	0.519×10^5	0.497×10^5
$\check{O}_t$	0.253×10^8	0.212×10^8	0.268×10^8	0.146×10^8	0.600×10^4	–	0.558×10^5	0.504×10^5
Λ	0.707	0.576	0.995	0.780	0.032	–	1.055	1.160
Rm	164	149	138	102	64	50	113	102
Nu_i	2.125	1.926	2.275 (2.443)	1.730	11.28 (10.63)	9.577	13.09 (13.33)	11.95 (10.44)
Nu_o	1.067	1.055	1.075 (1.092)	1.046	1.656 (1.615)	1.423	1.753 (2.074)	1.566 (1.415)

TABLE 1. Time-averaged global properties of dynamos with various velocity and thermal boundary conditions as follows. **A**: stress-free and fixed-temperature, **B**: stress-free and fixed-flux, **C**: no-slip and fixed-temperature, **D**: no-slip and fixed-flux. The predominant symmetry type is indicated with "D" if dipolar, "Q" if quadrupolar and "–" if the dynamo is decaying. Values for non-magnetic convection are given in brackets where available.

the absence of the magnetic field such that the solution diverges. This result emphasizes the smoothing effect of the magnetic field in cases with $P_m < 1$. At high Prandtl numbers the kinetic energies in dynamo cases are always a bit lower than in the corresponding non-magnetic cases. Only the mean poloidal energy densities measuring the strength of axisymmetric meridional circulations and in some instances the mean toroidal energy density appear to be enhanced by the dynamo action. This result seems to be independent of the thermal boundary conditions and agrees generally with the results displayed in figure 9. This same situation appears to hold in the case of no-slip conditions at the boundaries even for Prandtl numbers of the order unity or less as is evident from case (c) of table 1. This property is in stark contrast to the case of stress-free boundaries where the energy densities of the non-axisymmetric components are usually strongly amplified by the dynamo as is evident from figure 16 and others of SB05. Only the energy of differential rotation is reduced by the Lorentz force in both, the no-slip and the stress-free cases. The same observations apply in the comparison of results obtained by Christensen et al. (1999) for the two types of boundary conditions.

The analogy between the results for no-slip boundaries and for stress-free boundaries at high Prandtl numbers is not surprising if it is remembered that the presence of Ekman layers at the rigid boundaries increases strongly the viscous dissipation and thus the effective Prandtl number relative to the stress-free case. The analogy holds also for the energy of the axisymmetric dipolar field which exceeds the energies of all other components of the magnetic field in the no-slip cases (c) and (d) as well as in the stress-free cases (g) and (f) at $P = 20$ in table 1.

Characteristic structures of velocity and magnetic fields of the examples of table 1 are shown in figure 16. Only a quarter of the respective circles is used to visualize the differential rotation and the axisymmetric component of Θ since these fields are nearly symmetric relative to the equatorial plane.

7. Concluding remarks

It is popular in dynamo theory to neglect the momentum advection terms in the equation of motion (Glatzmaier and Roberts, 1995a; Jones, 2003) since they are undoubtedly small in comparison with the Coriolis force. In view of the results of section 4 and the analysis of SB05 this neglect can be well justified in the limit of high Prandtl numbers and to some extent in the presence of strong influences of Ekman layers. It is not surprising that dynamos without momentum advection terms exhibit the typical features of high Prandtl number dynamos such as a dominant axial dipolar magnetic field with strong toroidal flux tubes in the polar regions. But for values of P of the order unity or lower and stress-free boundary conditions the neglect of the momentum advection terms is less well satisfied since quite different types of dynamos with dominant non-axisymmetric components of the field are found as seen in figure 6 and even more dramatically in corresponding figures of SB05. The transition to dynamos with dominating higher multipoles found by Kutzner and Christensen (2002) at higher Rayleigh numbers in the presence of no-slip boundaries must probably be attributed also to the momentum advection terms. In spite of their smallness they can drive the geostrophic differential rotation which is the most easily exited component of fluid motion. Neither Coriolis force, nor pressure gradient, nor buoyancy force can drive a geostrophic differential rotation. Only the Lorentz force enters as a possible competitor. The latter force usually tends to damp the differential rotation according to Lenz' rule since the mean toroidal field is generated by it. It seems that the separation of dynamos into these two classes will persist when τ increases. But further investigations of this point are desirable.

The analysis of this paper has focused on cases of moderate Rayleigh numbers where the effects of the particular choice of the basic temperature profile are still noticeable. Other authors have employed temperature profiles without internal heating and Kutzner and Christensen (2000) have analyzed ways in which different basic profiles affect properties of convection driven dynamos. Similarly a fixed radius ratio has been used in the present paper in order to avoid the discussion of even more parameters. While convection driven dynamos in rotating spherical shells with a radius ratio of 0.4 or lower typically exhibit dipole and quadrupole components of the magnetic field that are axially oriented, this situation tends to change as higher values of the radius ratio are used. Depending on initial conditions Aubert and Wicht (2004) find in the case of a radius ratio 0.5 dynamos with an equatorial dipole or with an axial dipole for identical values of the parameters of the problem. Clearly, in applications to cases of particular planetary or stellar magnetic fields parameters that have been fixed in the present analysis are likely to play an important role.

REFERENCES

Aubert, J., and Wicht, J. 2004 Axial vs. equatorial dipolar dynamo models with implications for planetary magnetic fields. *Earth Plan. Sci. Lett.* **221**, 409–419.

Busse, F.H. 2002 Convection flows in rapidly rotating spheres and their dynamo action. *Phys. Fluids* **14** 1301–1314.

Busse, F.H., Grote, E., and Simitev, R. 2003 Convection in rotating spherical shells and its dynamo action, pp. 130-152 *in "Earth's Core and Lower Mantle", C.A.Jones, A.M.Soward and K.Zhang, eds., Taylor and Francis*

Busse, F.H., Grote, E., and Tilgner, A. 1998 On convection-driven dynamos in rotating spherical shells. *Studia geoph. et geod.* **42**, 211–223.

Busse, F.H., and Simitev, R. 2000 Inertial convection in rotating fluid spheres. *J. Fluid Mech.* **498** 23–30.

Busse, F.H., and Simitev, R. 2005 Convection in rotating spherical fluid shells and its dynamo states. *in Fluid Dynamics and Dynamos in Astrophysics and Geophysics, eds. A.M. Soward, C.A. Jones, D.W. Hughes, N.O. Weiss, CRC Press, pp. 359–392.*

Christensen U 2002 Zonal flow driven by strongly supercritical convection in rotating spherical shells. *J. Fluid Mech.* **470** 115–133.

Christensen, U., Olson, P., and Glatzmaier, G.A. 1999 Numerical Modeling of the Geodynamo: A Systematic Parameter Study. *Geophys. J. Int.* **138** 393–409.

Glatzmaier, G.A., Roberts, P.H., 1995 A three-dimensional self-consistent computer simulation of a geomagnetic field reversal. *Nature* **377**, 203-209.

Glatzmaier, G.A., and Roberts, P.H. 1995a A three-dimensional convection dynamo solution with rotating and finitely conducting inner core and mantle. *Phys. Earth Plan. Inter.* **91** 63–75.

Grote, E., and Busse, F.H. 2000 Hemispherical dynamos generated by convection in rotating spherical shells. *Phys. Rev.* **E 62** 4457–4460.

Grote, E., and Busse, F.H. 2001 Dynamics of convection and dynamos in rotating spherical fluid shells. *Fluid Dyn. Res.* **28** 349–368.

Grote, E., Busse, F.H., and Simitev R. 2001 Buoyancy driven convection in rotating spherical shells and its dynamo action, pp. 12-34 *in "High Performance Computing in Science and Engineering '01", E. Krause, W. Jäger, (eds.), Springer.*

Grote, E., Busse, F.H., and Tilgner, A. 1999 Convection-driven quadrupolar dynamos in rotating spherical shells. *Phys. Rev.* **E 60** R5025–R5028.

Grote, E., Busse, F.H., and Tilgner, A. 2000 Regular and chaotic spherical dynamos. *Phys. Earth Planet. Inter.* **117** 259–272.

Jones, C.A., 2003 Dynamos in planets. In: Thompson M J, Christensen-Daalsgard J. (eds.) *Stellar Astrophysical Fluid Dynamics* Cambridge University Press, pp. 159-176.

Knaack, R., Stenflo, J. O., and Berdyugina, S. V. 2004 Periodic oscillations in the north-south asymmetry of the solar magnetic field. *Astron. & Astrophys.* **418** L17-L20.

Kutzner, C., and Christensen, U.R. 2000 Effects of driving mechanisms in geodynamo models. *Geophys. Res. Lett.* **27** 29–32.

Kutzner, C., and Christensen, U.R. 2002 From stable dipolar towards reversing numerical dynamos. *Phys. Earth Planet. Inter.* **131** 29–45.

Moffatt, H.K., 1978 *Magnetic field generation in electrically conducting fluids* Cambridge University Press.

Olson, P., and Christensen, U.R. 2002 The time-averaged magnetic field in numerical dynamos with non-uniform boundary heat flow. *Geophys. J. Int.* **151** 809-823.

Parker, E. N. 1955 Hydromagnetic dynamo models. *Astrophys. J.* **122** 293-314.

Roberts, P.H., 1972 Kinematic Dynamo Models. *Phil. Trans. Roy. Soc. London* **A272** 663-698

Schrinner, M., Raedler, K., Schmitt, D., Rheinhardt, M., and Christensen, U. 2005

Mean-field view on rotating magnetoconvection and a geodynamo model. *Astronom. Nachr.* **326** 245–249.

Simitev, R. and Busse, F.H. 2003 Patterns of convection in rotating spherical shells. *New J. Phys.* **5** 97.1–97.20.

Simitev, R. and Busse, F.H. 2005 Prandtl-number dependence of convection-driven dynamos in rotating spherical fluid shells. *J. Fluid Mech.* **532** 365-388.

Sparrow, E.M., Goldstein, R.J., and Jonsson, V.K. 1964 Thermal instability in a horizontal fluid layer: effect of boundary conditions and non-linear temperature profile. *J. Fluid Mech.* **18** 513–528.

Tilgner, A. 1999 Spectral Methods for the Simulation of Incompressible Flows in Spherical Shells. *Int. J. Numer. Meth. Fluids* **30** 713-724.

Tilgner, A., and Busse, F.H. 1997 Finite amplitude convection in rotating spherical fluid shells. *J. Fluid Mech.* **332** 359–376.